Laser-Activated Voltammetry. Mechanism of Aqueous Iodide Oxidation at Platinum Electrodes: Theory and Experiment

Richard P. Akkermans, Qiu Fulian, Sarah L. Roberts, Marco F. Suárez, and Richard G. Compton*

Physical and Theoretical Chemistry Laboratory, Oxford University, South Parks Road, Oxford, OX1 3QZ, U.K.

Received: June 2, 1999; In Final Form: August 4, 1999

The mechanism of iodide oxidation on platinum electrodes is investigated using laser-activated voltammetry under both channel flow and no flow conditions together with independent in situ atomic force microscopy (AFM) measurements. Laser activation using a 10 Hz pulsed Nd:YAG 532 nm laser is shown to remove bulk iodine from the electrode surface so that under sustained pulsed irradiation a steady-state surface evolves at which the iodide oxidation can be reproducibly studied. When the concentration and flow rate dependence of the voltammetric wave shape are modeled, the mechanism is shown to be the following: $2I^-$ (aq) $- 2e^- \rightleftharpoons I_2$ (aq) (i); I_2 (aq) $+ I^-$ (aq) $\rightleftharpoons I_3^-$ (aq) (ii); I_2 (aq) $\rightleftharpoons I_2$ (s) (iii); I^- (aq) $+ I_2$ (s) $\rightarrow I_3^-$ (aq) (iv), where the formal redox potential for reaction i is 0.358 V vs SCE in 0.1 M H_2SO_4, the equilibrium constant for reaction ii is 580 M^{-1} with a forward rate constant of 1×10^5 mol^{-1} cm^3 s^{-1}, the solubility of I_2 (reaction ii) is 1.85×10^{-3} M, and the heterogeneous rate constant for reaction iv is 1.6×10^{-3} cm s^{-1}.

Introduction

The surface modification of both single-crystal and polycrystalline platinum with iodine has been the subject of considerable structural and electrochemical study.[1−7] It has been reported that aqueous iodide undergoes spontaneous oxidation upon chemisorption to form a layer of zerovalent atomic iodine on platinum electrodes[8] at potentials between 0 and +0.4 V vs SCE. At higher potentials, further deposition of atomic iodine leads to the formation of molecular iodine, which can either form a solid deposit of iodine[9,10] or dissolve into the solution phase. The exact mechanism of how molecular iodine is formed from atomic iodine is not yet fully understood.[11] Moreover, iodine formed electrochemically on the platinum electrode surface by the oxidation of aqueous iodide changes the conductivity and kinetic properties of the electrode in a complicated fashion.[11] Electrochemical iodine growth has been studied by optical microscopy,[12] surface reflectance measurements,[13] surface-enhanced Raman spectroscopy,[14] atomic force microscopy,[15] and scanning tunneling microscopy.[16] Various electrochemical mechanisms of iodine formation have been summarized by Dané et al.;[17] however, the formation of bulk iodine necessarily complicates the interpretation of voltammetric data not least because of the constantly changing electrode condition as voltammetry proceeds.

Recently, the use of lasers to keep electrode surfaces clean and activated has become increasingly common. Watanabe and co-workers[18] used a relatively high-power infrared laser source to maintain fresh platinum and gold electrode surfaces by physically removing the top layer of electrode surface every few seconds via the phenomenon of "laser ablation".[18] This followed work by McCreery and colleagues who used high-intensity, in situ infrared laser pulses to activate the surface and increase heterogeneous electron-transfer kinetics at glassy carbon and platinum electrodes.[19−26] Oltra et al. have additionally used laser pulses to depassivate an iron electrode under the hydrodynamic conditions of a channel flow cell,[27] while Hinoue et al. used an argon ion laser to examine the effect of heating on the electron-transfer process of Fe(II/III) aqueous species in a flow system.[28] It is important to note that these[18−27] experiments used laser illumination solely to activate or refresh the electrode surface but not to provide direct chemical effects and a contrast can be drawn with situations where either solution-phase species absorb laser light to form electronically excited species, which then lead to electrochemical processes[29] or where irradiation of a semiconducting electrode is used to generate charge carriers.[30]

In this work laser-*activated* voltammetry (LAV) is employed with and without enforced hydrodynamic flow in order to control the buildup of solid iodine formed by iodide oxidation on platinum electrodes. The term *activated* is used to distinguish the surface-cleaning and current enhancement effects obtained while maintaining an essentially undamaged electrode from the drastic current fluctuations and major electrode damage associated with the *ablation* technique as employed, for example, by Watanabe et al.[18] Under high-energy pulsed ablation conditions, large fluctuating current spikes are produced as a consequence of the large temperature jumps associated with major electrode structural changes.[31] This electrode damage occurs when the laser pulses have sufficient energy to cause localized surface melting or even vaporization.[32,33]

In the following, *laser-activated voltammetry* (LAV) using a 10 Hz pulsed Nd:YAG laser at 532 nm is performed in order to investigate the mechanism of the electrochemical oxidation of aqueous iodide anions at a platinum electrode, under both stationary and hydrodynamic channel flow conditions. Under the latter conditions numerical modeling of the channel flow voltammetry gives qualitative mechanistic inferences together with quantitative kinetic data. Further, atomic force microscopy (AFM) is utilized to visualize the growth of bulk iodine deposits on the electrode surface.

Finally the introduction of ultrasound into electrochemical

* To whom correspondence should be sent. E-mail: richard.compton@chemistry.oxford.ac.uk.

10.1021/jp991778d CCC: $18.00
Published on Web 09/11/1999

systems has many noted benefits,[34,35] including extremely enhanced mass transport resulting from acoustic streaming[36] or microjetting[37] and electrode activation arising from cavitational cleaning.[38] Additionally, sonication has been used to permit the electrochemical study of essentially water-insoluble organic species in aqueous solution.[39,40] The use of ultrasound to induce an emulsion between water and dichloromethane is investigated for the purposes of dissolving largely water-insoluble redox products on the electrode surface and trapping them in the organic phase.

Theory

Oxidation of Aqueous Iodide in a Channel Flow Cell. We consider first the voltammetric behavior of the aqueous I^-/I_2 system in the limit of low concentrations[7] where iodine is formed at concentrations below its solubility and at levels such that the formation of I_3^- can be neglected. The electrochemically reversible oxidation process is as follows,

$$I^-(aq) - e^- \rightleftharpoons \frac{1}{2}I_2(aq) \tag{1}$$

The above process describes the sustained conversion of I^- to I_2 under the conditions of hydrodynamic voltammetry. The intermediary of species such as adsorbed iodine atoms, I_{ads}, in the above process[17] is neglected, consistent with the observed electrochemical reversibility of the I^-/I_2 system (vide infra). Application of the Nernst equation to eq 1 gives the following expression:

$$\left(\frac{[I_2]_0}{[I_2]^*}\right)^{1/2}\Big/\left(\frac{[I]_0}{[I^-]^*}\right) = \exp(\theta) \tag{2}$$

where $\theta = [F/(RT)](E - E^{\circ\prime})$, $[I^-]_0$ and $[I_2]_0$ are the surface concentrations and $[I^-]^*$ and $[I_2]^*$ the thermodynamic standard states of iodide and iodine, respectively, F is the Faraday constant, E is the electrode potential, and $E^{\circ\prime}$ is the formal potential of the I_2/I^- redox couple. For the case of voltammetry conducted at a hydrodynamic electrode this leads to the following result for the current (I)−voltage (θ) behavior:[30−31]

$$\ln\left\{\left(\frac{I_{Lim}}{I}\right)^{1/2} - \left(\frac{I}{I_{Lim}}\right)^{1/2}\right\} = -\theta - \frac{1}{2}\ln\left\{\frac{2D_{I_2}}{D_{I^-}}[I^-]_{bulk}\right\} \tag{3}$$

where I_{Lim} is the mass transport limited current, D is the relevant diffusion coefficient,[44] and $[I^-]_{bulk}$ is the bulk concentration of iodide. Equation 3 implies that the half-wave potential, $E_{1/2}$, where $I = I_{Lim}/2$ for the iodide oxidation, intrinsically varies with both the ratio (D_{I_2}/D_{I^-}) and the bulk concentration of iodide, even in the absence of any following homogeneous kinetics. Quantitatively,

$$-\frac{1}{2}\ln\left\{\frac{D_{I_2}}{D_{I^-}}[I^-]_{bulk}\right\} = \left(\frac{F}{RT}\right)(E_{1/2} - E^{\circ\prime}) = \theta_{1/2} \tag{4}$$

so that increasing the concentration of I^- in solution shifts the half-wave potential of the oxidation wave to less positive potentials.

In the low-concentration limit, the steady-state convection−diffusion equations describing the electrochemical process at a channel electrode are as follows.

$$D_{I^-}\frac{\partial^2[I^-]}{\partial y^2} - v_x\frac{\partial[I^-]}{\partial x} = 0 \tag{5}$$

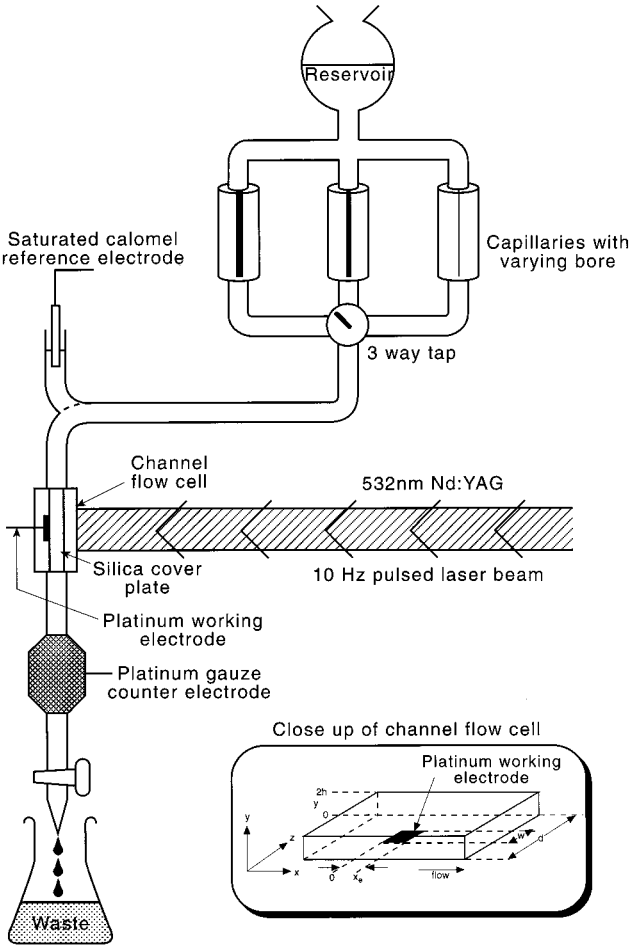

Figure 1. Gravity-fed channel flow apparatus used in laser-activated voltammetry experiments. Inset: schematic diagram of the channel flow cell used in this work.

$$D_{I_2}\frac{\partial^2[I_2]}{\partial y^2} - v_x\frac{\partial[I_2]}{\partial x} = 0 \tag{6}$$

where x and y are defined in Figure 1. Under parabolic laminar flow conditions, v_x is defined quantitatively by

$$v_x = v_0\left(1 - \frac{(h-y)^2}{h^2}\right) \tag{7}$$

where v_0 is the central velocity in the channel and $2h$ is the cell height.

The boundary conditions relevant to the calculation of the current−voltage curve in the low concentration limit are

$$x < 0: \qquad [I^-] = [I^-]_{bulk} \tag{8}$$

$$0 < x < x_e,\ y = 0: \qquad [I_2]/[I^-]^2 = \exp(2\theta);\ [I_2] \le [I_2]_{sat} \tag{9}$$

$$0 < x < x_e,\ y = 0: \qquad 2D_{I_2}\frac{\partial[I_2]}{\partial y}\Big|_{y=0} = -D_{I^-}\frac{\partial[I^-]}{\partial y}\Big|_{y=0} \tag{10}$$

$$y = 2h: \qquad \frac{\partial[I^-]}{\partial y} = \frac{\partial[I_2]}{\partial y} = 0 \tag{11}$$

The coupled transport equations are solved using the backward implicit (BI) method[45] with back-to-back grids[46] to relate the species in the electrode reaction couple. These methods were

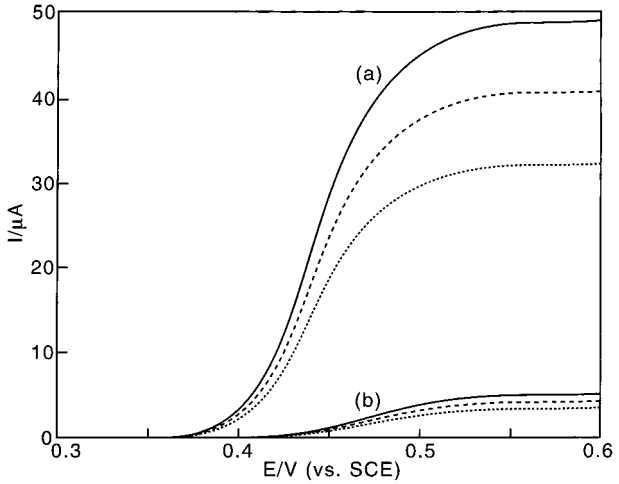

Figure 2. Simulated voltammograms at flow rates of 0.02 (···), 0.04 (- - -), and 0.07 (—) $cm^3\ s^{-1}$ for (a) 2.0 mM KI and (b) 0.2 mM KI. $K_2 = k_{het} = 0$ and $[I_2]_{sat} = 10$ mM, ensuring saturation is not reached.

used exactly as previously described[45,46] with the exception that since eq 9 is nonlinear, it cannot be used directly to define electrode surface concentrations of I^- and I_2. A linearization procedure[47,48] is employed here to calculate the concentrations of I^- and I_2 at the electrode surface. It is

$$\frac{[I_2]_{K+1}}{2[I^-]_K[I^-]_{K+1} - [I^-]_K{}^2} = \exp(2\theta) \tag{12}$$

where K is the grid number in the x direction. The electrode current, I, is then evaluated from the following expression

$$I = wF\int_0^{x_e} D_{I^-}\left[\frac{\partial[I^-]}{\partial y}\right]_{y=0} dx \tag{13}$$

where w is the width of the electrode as defined in Figure 1.

Figure 2 shows computed waves for iodide oxidation at two different concentrations (0.2 and 2 mM) and for three different typical flow rates (0.02, 0.04, and 0.07 $cm^3\ s^{-1}$) for a channel electrode of typical dimensions (electrode length 0.18 cm, electrode width 0.18 cm, cell depth 0.04 cm, and cell width 0.6 cm). Note that the simulations predict the variation of $E_{1/2}$ with concentration anticipated by eq 4. Simulations over the concentration range $0.1 < [I^-]_{bulk}/mM < 2$ gave quantitative agreement with this equation. In addition Tafel analysis of the simulated wave shapes conducted on the basis of eq 3 showed excellent agreement with the predictions of analytical theory. Figure 3 shows typical Tafel plots for 0.2 and 2 mM iodide concentrations; the observed slopes of −1.000 and −1.001, respectively, are in quantitative agreement with eq 3.

We next consider the well-established formation of triiodide (I_3^-) from the reaction between *aqueous* iodide and iodine.[17] The reaction mechanism now becomes

$$2I^-(aq) - 2e^- \rightleftharpoons I_2(aq) \tag{14}$$

$$I^-(aq) + I_2(aq) \underset{k_b}{\overset{k_f}{\rightleftharpoons}} I_3^-(aq) \tag{15}$$

where k_f and k_b are forward and backward rate constants, respectively, for the generation of the triiodide reaction. The modified steady-state convection−diffusion equations include the new species as follows.

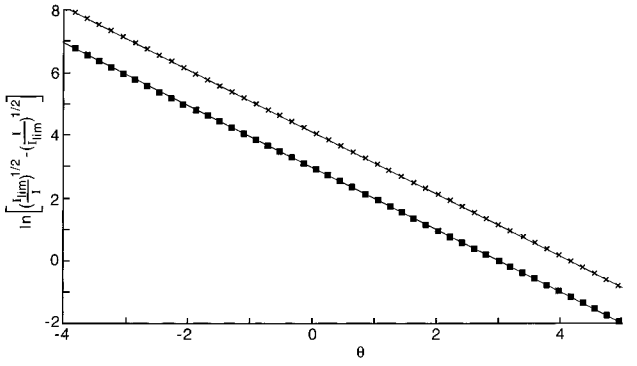

Figure 3. Tafel analysis plots for the 0.04 $cm^3\ s^{-1}$ waves in Figure 2: (×) 0.2 mM; (■) 2 mM. The slopes of −1.000 and −1.001 respectively agree quantitatively with eq 3.

$$D_{I^-}\frac{\partial^2[I^-]}{\partial y^2} - v_x\frac{\partial[I^-]}{\partial x} - k_f[I^-][I_2] + k_b[I_3^-] = 0 \tag{16}$$

$$D_{I_2}\frac{\partial^2[I_2]}{\partial y^2} - v_x\frac{\partial[I_2]}{\partial x} - k_f[I^-][I_2] + k_b[I_3^-] = 0 \tag{17}$$

$$D_{I_3^-}\frac{\partial^2[I_3^-]}{\partial y^2} - v_x\frac{\partial[I_3^-]}{\partial x} + k_f[I^-][I_2] - k_b[I_3^-] = 0 \tag{18}$$

Further boundary conditions are now applicable to triiodide,

$$0 < x < x_e,\ y = 0: \qquad D_{I_3^-}\frac{\partial[I_3^-]}{\partial y} = 0 \tag{19}$$

$$y = 2h: \qquad \frac{\partial[I_3^-]}{\partial y} = 0 \tag{20}$$

It is readily shown using analytical arguments[49] that the dimensionless shift in half-wave potential, $\theta_{1/2}$, must be a unique function of two normalized parameters. First, the normalized second-order rate constant is defined as

$$K_2 = k_f[I^-]_{bulk}\left(\frac{4h^4x_e{}^2d^2}{9v_f{}^2D_{I^-}}\right)^{1/3} \tag{21}$$

where v_f is the volume flow rate and d is the cell width. Second, a dimensionless equilibrium constant, K, for the chemical reaction is defined as

$$K = \frac{1}{K_{eq}[I^-]_{bulk}} \tag{22}$$

where K_{eq} ($=k_f/k_b$) is the equilibrium constant for the chemical reaction given in eq 15. Figure 4 shows the simulated behavior in terms of a working surface relating $\theta_{1/2}$ to K_2 and K. In addition consideration of reactions 14 and 15 leads one to expect that as K_{eq} and K_2 are increased, then the effective number of electrons transferred per iodide ion (N_{eff}) will fall below 1, since iodine released into solution will "trap" incoming iodide as triiodide before it can react at the electrode. Figure 5 shows a working surface relating N_{eff} to K and K_2. It can be seen that N_{eff} does indeed decrease when triiodide formation is favored both kinetically and thermodynamically.

We consider next the equilibrium between aqueous iodine and solid iodine on the electrode surface. At higher concentrations of iodide (greater than ca. 3 mM) the iodine formed at

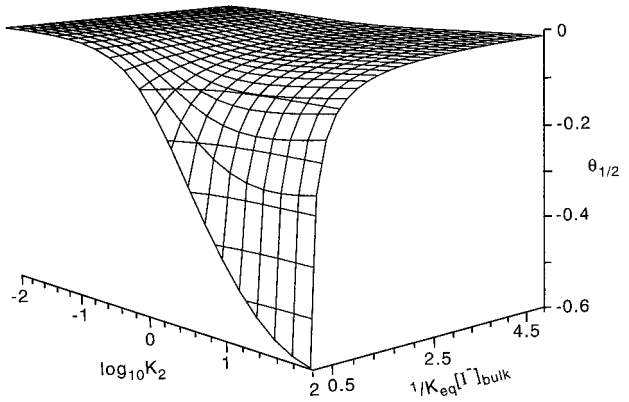

Figure 4. Working surface for the effect of K_2 and K on $\theta_{1/2}$. $[I_2]_{sat} = 1.2$ mM and $k_{het} = 0$ cm s^{-1}.

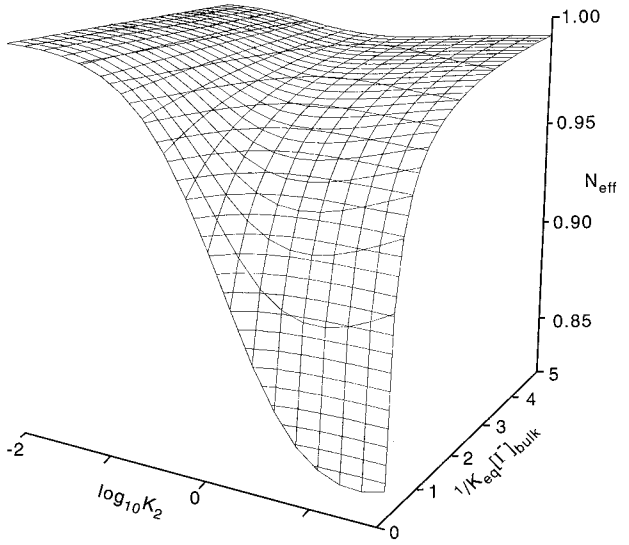

Figure 5. Working surface for the effect of K_2 and K on N_{eff}. $[I_2]_{sat} = 1.2$ mM and $k_{het} = 0$ cm s^{-1}.

the electrode forms a locally saturated solution within the diffusion layer. As the concentration of iodine increases such that it exceeds its solubility, i.e., $[I_2] > [I_2]_{sat}$, crystallization can occur on the platinum surface and the following boundary condition applies

$$0 < x < x_e,\ y = 0: \qquad [I_2]_{sat}/[I^-]^2 = \exp(2\theta);\ [I_2] \geq [I_2]_{sat} \tag{23}$$

Equation 10 may be used approximately under these new conditions provided the net precipitation rate is small compared with the overall fluxes at the electrode surface.

Figure 6 shows simulated voltammetry for a 6 mM iodide solution for varying hypothetical values of iodine saturation ($[I_2]_{sat}$). The significant effect of the iodine solubility on both the wave shape and the total magnitude of the voltammetric wave is evident. Interestingly, N_{eff} is controlled by the solubility because of the influence of that parameter on the triiodide levels in the diffusion layer. The distinctive voltammetric wave shape in the presence of solid iodine at the interface is characteristic of precipitation but might, for example, be, in this system, easily mistaken for the following reactions as separate electrode processes:

$$I^- - \frac{2}{3}e^- \rightarrow \frac{1}{3}I_3^- \tag{24}$$

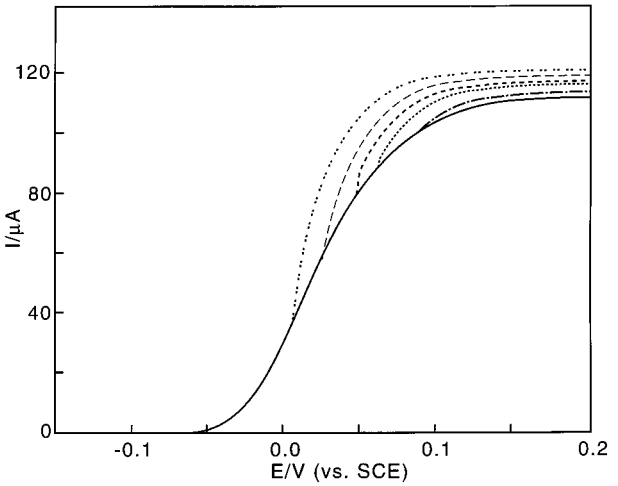

Figure 6. Simulated voltammograms for 6 mM KI at a flow rate of 0.04 cm^3 s^{-1} for hypothetical iodine saturation concentrations of 0.5 (- - - -), 1 (— —), 1.5 (- - -), 2 (•••), 3 (— •), and 4 (—) mM. $k_f = 1 \times 10^5$ mol^{-1} cm^3 s^{-1}, and $k_{het} = 0$ cm s^{-1}.

and

$$I^- - e^- \rightarrow \frac{1}{2}I_2 \tag{25}$$

Last, we consider a final possible complication: once iodine is present on the electrode surface, there is the possibility of dissolution in iodide-containing solution[11] to form aqueous triiodide ions according to the following heterogeneous reaction, which is in competition with the charge transfer in eq 1

$$I^-(aq) + I_2(s) \xrightarrow{k_{het}} I_3^-(aq) \tag{26}$$

where k_{het} is the heterogeneous rate constant (cm s^{-1}) for the reaction. Simulation of this requires a change of the electrode surface boundary condition for triiodide diffusion in eq 19 to

$$0 < x < x_e,\ y = 0: \qquad D_{I_3^-}\frac{\partial[I_3^-]}{\partial y} = -k_{het}[I^-] \tag{27}$$

and correspondingly changes the expression for the current from eq 13 to

$$I = wF\int_0^{x_e}\left\{D_{I^-}\left[\frac{\partial[I^-]}{\partial y}\right]_{y=0} - k_{het}[I^-]_{y=0}\right\}dx \tag{28}$$

Figure 7 shows simulated voltammograms for varying k_{het} and clearly shows the change in wave shape as k_{het} increases. This reflects the competition between eqs 1 and 26 alluded to above and the added injection of triiodide into the diffusion layer.

Experimental Section

Laser-activated voltammetry and chronoamperometry in nominally stationary solution was conducted in the three-electrode cell shown in Figure 8. For most experiments this utilized a 1 mm diameter platinum disk working electrode embedded in a Perspex window set in a Teflon mount, a saturated calomel electrode (SCE, Radiometer, Copenhagen) as a reference electrode, and a graphite rod as the counter electrode. The cell volume was approximately 15 cm^3. The bulk solution temperature was measured using a platinum resistance thermometer and was 20 ± 2 °C in all cases. The temperature during

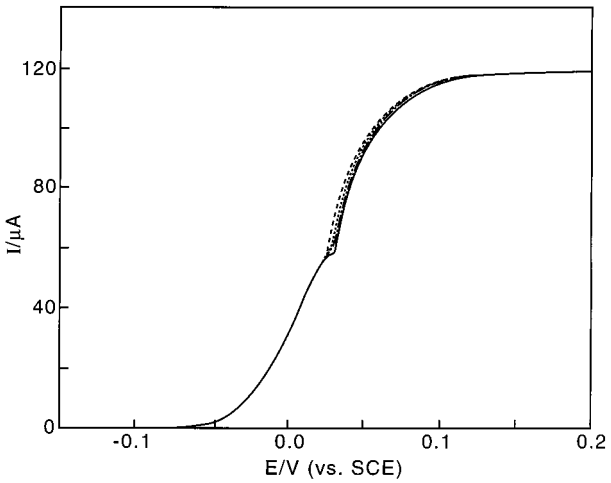

Figure 7. Simulated voltammograms for 6 mM KI at a flow rate of 0.04 $cm^3\ s^{-1}$, $k_f = 1 \times 10^5\ mol^{-1}\ cm^3\ s^{-1}$, and $[I_2]_{sat} = 1$ mM for hypothetical values of k_{het} of 0 (- - -), 0.5 (•••), 1 (— •), and 1.5 (—) × 10^{-3} cm s^{-1}.

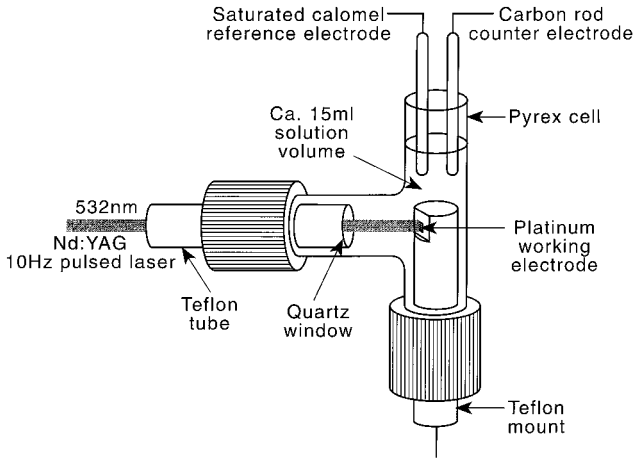

Figure 8. Experimental arrangement employed for laser-activated voltammetry in stationary solution.

individual runs was found to increase by less than 0.2 °C, demonstrating a minimal overall bulk heating effect by the laser.

Voltammetry under gravity flow conditions was performed using the apparatus shown in Figure 1. It utilized optically transparent channel flow cells as detailed elsewhere[29] and either a platinum 2 mm diameter disk or a platinum 2 mm square electrode maintained in a fixed position relative to the incident laser beam.

The light source employed was a LAB 130 Q-switched Nd:YAG laser (Spectra Physics Lasers, Inc., CA) operating in frequency-doubled mode at a wavelength of 532 nm and pulsed at 10 Hz. Lenses and optics housings were supplied by Newport Corporation and mirrors obtained from Comar Instruments (Cambridge, U.K.). The beam was reduced to 3.0 or 4.0 mm in diameter by means of passage through a fixed diameter aperture before being passed into the LAV cell. The laser power was determined with a Gentec ED-200LA detector head in conjunction with a Gentec SUN series EM-1 energy meter (Gentec, CA). The power recorded by the meter was a time-average reading and not the power associated with individual laser pulses, which have a half-height width of ca. 8 ns and a pulse repetition rate of 10 Hz. By use of the fixed diameter of the beam, it was then possible to calculate laser *intensities* averaged over the full electrode area. Good homogeneity of illumination was achieved. Typical experiments were performed in the range 0.1−0.8 W cm^{-2}.

The source of ultrasound employed was a 20 kHz titanium-tipped ultrasonic horn probe of 13 mm diameter (Sonics & Materials). Insonation experiments were conducted using a 250 mL sonovoltammetric cell at 20 °C, which has been previously described.[50] Ultrasound power levels up to 50 W cm^{-2} were employed.[51,52]

A computer-controlled PGSTAT20 Autolab potentiostat (Eco-Chemie, Utrecht, The Netherlands) was employed to control the potential applied at the working electrode in all experiments. The dimensions of the platinum electrodes were accurately measured using a travelling microscope. Electrodes were carefully polished using diamond lapping compounds (Kemet, Kent, U.K.) of decreasing size to 0.1 μm before use.

Potassium ferricyanide, potassium ferrocyanide, potassium iodide (all BDH), ruthenium hexaammine trichloride, and sulfuric acid (both Aldrich) were all of the highest commercially available purity and used as received. Aqueous solutions were prepared using Elgastat (Elga, High Wycombe, Bucks) UHQ grade water of resistivity not less than 18 MΩ cm. All solutions were thoroughly purged with argon (Pureshield) to remove any dissolved oxygen prior to electrolysis.

Atomic force microscopy (AFM) surface imaging of a platinum disk was performed on a TopoMetrix TMX 2010 Discoverer system in contact mode (typically 10 Hz scan rate) with TopoMetrix standard AFM probes (no. 15-20).

UV−visible spectroscopy was carried out on a Perkin-Elmer UV2 spectrometer with a quartz cuvette of path length 1 cm, while simulations were performed using computer programs written in FORTRAN 77 and executed on a Silicon Graphics workstation.

Results and Discussion

We consider first the measurement of the formal potential of the electrode process given in eq 1. Chronopotentiometric experiments were performed with a platinum electrode immersed in a 50 mL solution of 0.2506 mM iodine in 0.1 M H_2SO_4 with six small additions of 0.5 mL aqueous 1.07 mM iodide every 60 s to measure the change in cell potential relative to the SCE as a function of concentration. Analysis of the results using the Nernst equation revealed a value of 0.358 ± 0.004 V (vs SCE) for the formal cell potential. This was in good agreement with literature values once corrected for SCE.[11]

We then obtained a value for the equilibrium constant, K_{eq}, of eq 15 by UV−visible spectroscopy. Stock solutions of 0.109 M KI and 0.752 mM I_2 in 0.1 M H_2SO_4 were mixed in various proportions and the absorption due to triiodide recorded (λ_{max} = 351 nm). Once calibrated by comparison with a standard solution of potassium triiodide, the equilibrium constant at 18 °C was calculated as 580 ± 20 M^{-1}. This compares favorably with the value of 620 M^{-1} (25 °C, 0.5 M H_2SO_4) reported in the literature.[17]

Next we consider the oxidation of iodide in aqueous sulfuric acid. This has been demonstrated to lead to the production of solid iodine when adequately high concentrations (greater than ca. 3 mM) of iodide are employed.[1,2,17,53−55] This formation of solid iodine occurs when the solubility of iodine is exceeded (1.1 mM in water at 25 °C).[56] The growth of electrochemically generated iodine on the platinum electrode surface was investigated by in situ AFM. While maintaining a potential of +0.56 V (vs SCE) at a platinum electrode immersed in aqueous potassium iodide solution, scans were taken at approximately minute intervals to probe the buildup of surface deposits. Figure

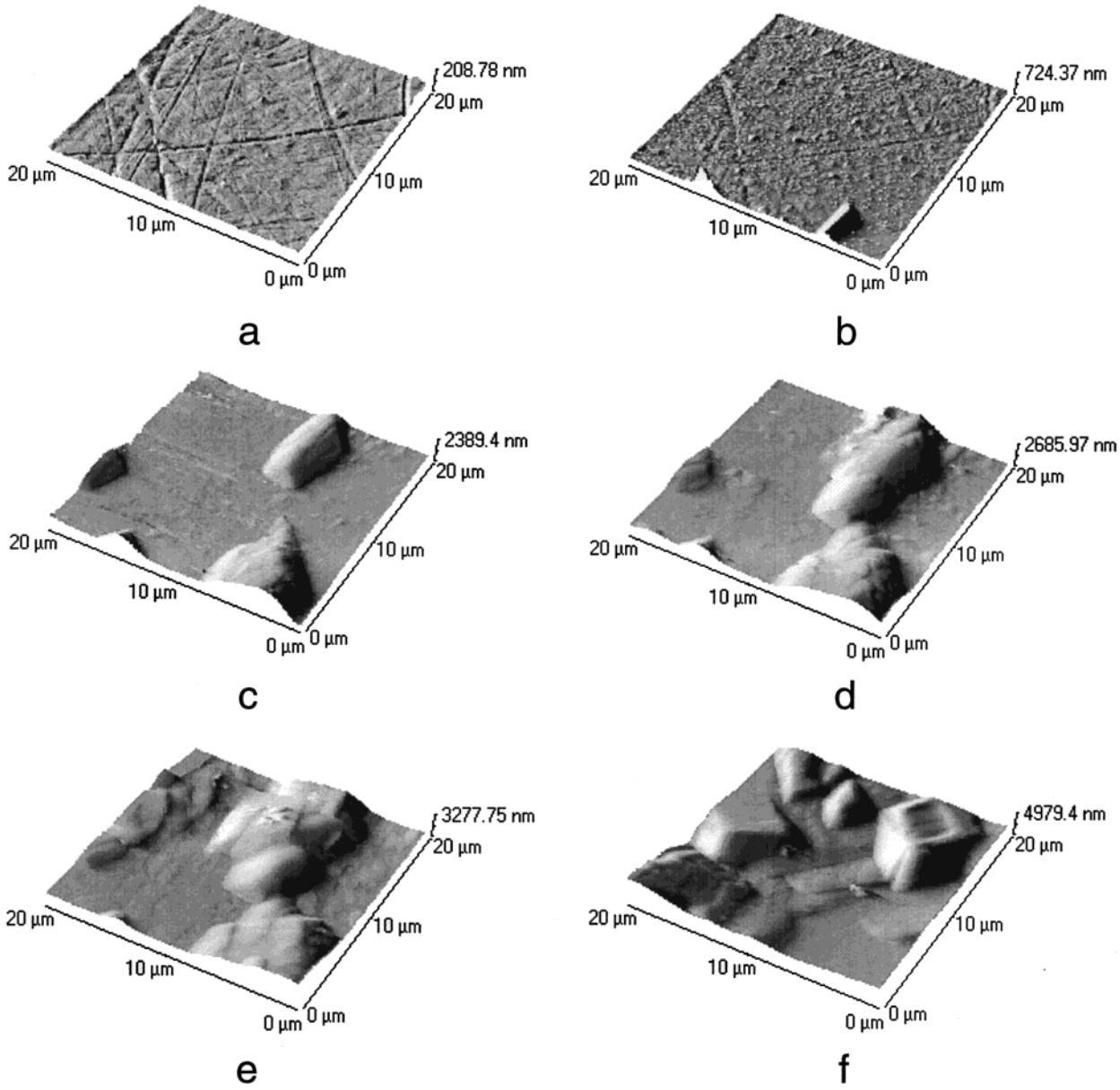

Figure 9. AFM pictures of a platinum electrode: (a) polished, (b) after 208 s, (c) after 416 s, (d) after 571 s, (e) after 728 s, all at 0.56 V in 3 mM KI, 0.01 M H_2SO_4, and (f) after 420 s at 0.56 V in 5 mM KI, 0.01 M H_2SO_4.

9 shows six AFM images: (a) a polished platinum electrode and the same electrode in a 3 mM solution of potassium iodide in 0.01 M H_2SO_4 after (b) 208 s, (c) 416 s, (d) 571 s, and (e) 728 s at 0.56 V vs SCE. The sixth scan (f) shows the surface after 420 s of oxidation at 0.56 V (vs SCE) for a 5 mM solution of potassium iodide in 0.01 M H_2SO_4. The growth of crystals on the electrode surface is evident.

Introduction of laser irradiation to the electrode surface can be expected to interfere with these surface deposition processes. Linear sweep voltammetry in nominally stationary solution was performed at a variety of scan rates, iodide concentrations, and laser intensities to probe the surface cleaning properties of laser activation. Figure 10 shows a typical linear sweep voltammogram for the oxidation of 10 mM potassium iodide in 0.125 M H_2SO_4. In the absence of laser illumination (b) the formation of iodine appears as the current peak at ca. 0.48 V vs SCE.[2] This leads to partial passivation of the electrode, making quantitative interpretation a challenging exercise.[55] During 300 mW cm^{-2} illumination (a) a sustained transport-limited current is observed due to a small amount of thermal convection at the

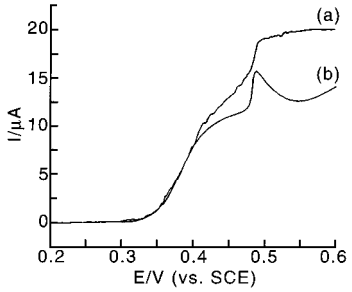

Figure 10. Linear sweep voltammograms at 5 mV s^{-1} for the oxidation of 10 mM potassium iodide in 0.125 M H_2SO_4 on a 1 mm diameter Pt disk electrode under (a) dark and (b) 300 mW cm^{-2} laser-illuminated conditions.

electrode surface. This intensity is insufficient to cause ablation of the platinum surface immersed in aqueous electrolyte.[57]

The removal of solid iodine from the electrode surface is illustrated by Figure 11, which shows corresponding cyclic and linear sweep voltammograms measured under flow conditions of 1.0×10^{-3} cm^3 s^{-1} (a and b) and 6.9×10^{-3} cm^3 s^{-1} (c)

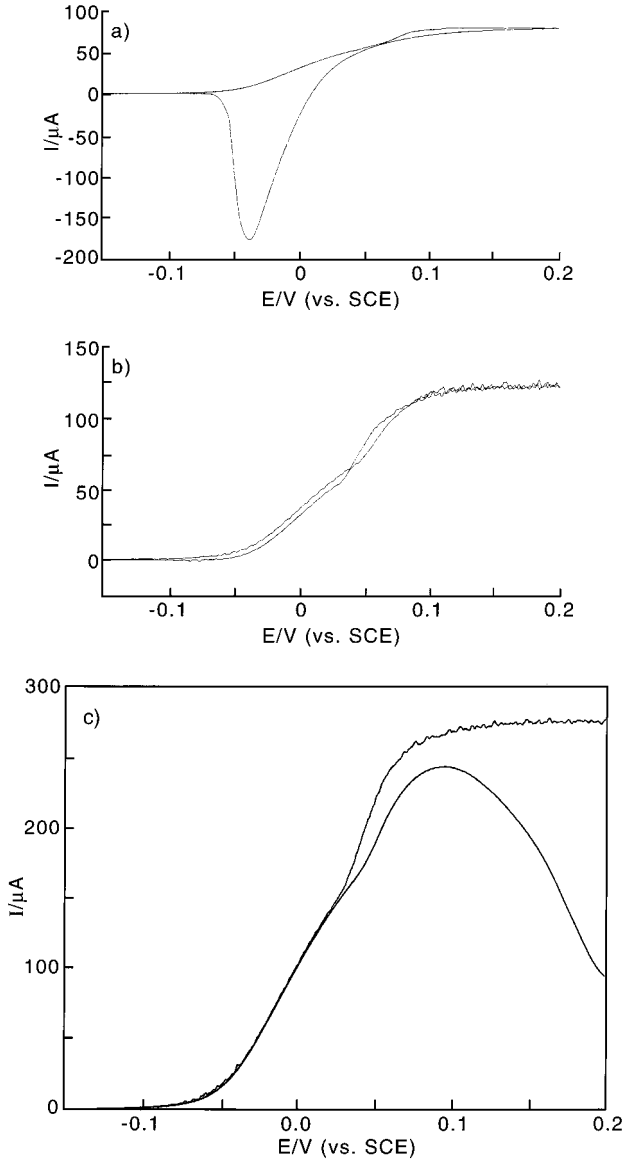

Figure 11. Voltammograms for 10.2 mM potassium iodide in 0.1 M H_2SO_4 at 5 mV s^{-1} on a 2 mm square Pt electrode under flow conditions: (a) cyclic voltammetry with no laser ($v_f = 1 \times 10^{-3}$ cm^3 s^{-1}); (b) cyclic voltammetry under 1200 mW cm^{-2} laser illumination ($v_f = 1 \times 10^{-3}$ cm^3 s^{-1}, smoothed trace); (c) linear sweep voltammetry at $v_f = 6.9 \times 10^{-3}$ cm^3 s^{-1} in the dark (lower trace) and under 1200 mW cm^{-2} laser illumination (upper, smoothed trace).

through a flow cell of cross-sectional area 0.6 cm × 0.04 cm using the apparatus shown in Figure 1. Trace a shows an appreciable stripping peak for the reduction of surface iodine to iodide. This was recorded under dark conditions. In contrast trace b shows the effect of 1200 mW cm^{-2} illumination on the same experiment. The reverse cyclic voltammetry scan essentially retraces the anodic sweep and a well-defined hydrodynamic wave is seen with no hysteresis. The ability of LAV to maintain an active electrode surface especially under convective conditions again offers considerable analytical value. Figure 11c shows the current falloff in the dark (lower trace) due to enhanced iodine deposition under faster flow conditions and the corresponding laser-activated (upper) trace with its mass transport limited current plateau suggesting the removal of the insulating surface iodine layer.

Next further laser-activated linear sweep voltammetry under gravity flow conditions was performed for comparison with simulated voltammetry. It is important to note that the mass

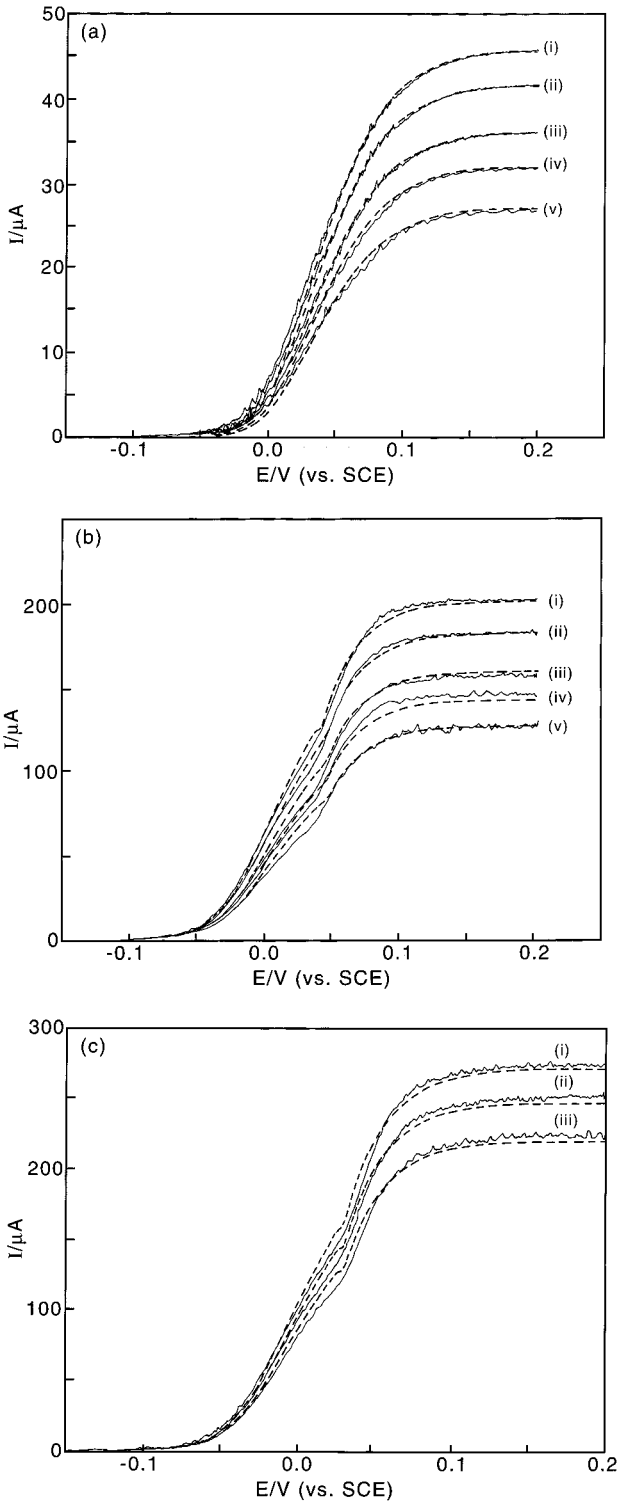

Figure 12. Simulated voltammograms for (a) 2.1, (b) 8.7, and (c) 10.4 mM KI at flow rates of (i) 0.069, (ii) 0.052, (iii) 0.034, (iv) 0.024, and (v) 0.015 cm^3 s^{-1}. $[I_2]_{sat} = 1.85$ mM, $k_f = 1 \times 10^5$ mol^{-1} cm^3 s^{-1}, and $k_{het} = 1.6 \times 10^{-3}$ cm s^{-1}.

transport limited waves are now controlled by the channel flow hydrodynamics, and laser intensities can be used such that no current enhancement due to electrode heating effects is seen. This was readily confirmed by performing linear sweep voltammetry on separate 5 mM solutions of ruthenium hexaammine trichloride and potassium ferrocyanide in 0.1 M KCl. At laser intensities below 1200 mW cm^{-2} and flow rates above 1.0×10^{-3} cm^3 s^{-1}, the laser and dark voltammograms coincided, except for some current spiking and noise on the laser traces.

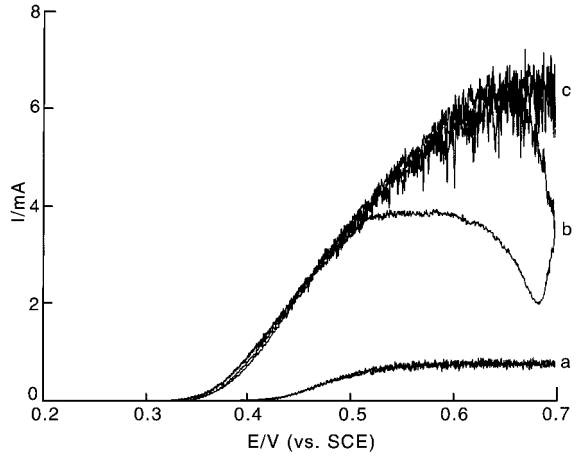

Figure 13. Sonocyclic voltammograms at 10 mV s^{-1} on a 6 mm Pt disk electrode for (a) 1 mM and (b) 10 mM KI in 0.125 M H_2SO_4. An intensity of 19 W cm^{-2} ultrasound was employed at a horn-to-electrode distance of 12 mm. Trace c is as for trace b except that 10% (v/v) of the aqueous solution was replaced with dichloromethane and emulsified.

The same was observed for solutions of iodide below ca. 3 mM, suggesting that for these simple reversible systems, the mass transport is dominated by the channel flow and not by laser-induced electrode heating. At high concentrations of iodide, the ability of the laser to keep the surface clean through removal of iodine results in a larger current being seen under illumination at a given flow rate as shown in Figure 11c.

Figure 12 shows 5 mV s^{-1} laser-activated linear sweep experimental waves for three different concentrations of aqueous iodide (2.1, 8.7, and 10.4 mM) at different flow rates and 1200 mW cm^{-2} laser intensity. These data were then simulated using the full theory outlined earlier. The measured values of υ_f, K_{eq}, $E^{\circ\prime}$, $[I^-]_{bulk}$, electrode area, temperature, and cell parameters were employed along with systematically optimized values for k_f, $[I_2]_{sat}$, and k_{het} to produce the best fit for wave position, shape, and limiting current. These optimized values were $(1.0 \pm 0.1) \times 10^5$ mol^{-1} cm^3 s^{-1}, $(1.85 \pm 0.10) \times 10^{-3}$ M, and $(1.6 \pm 0.2) \times 10^{-3}$ cm s^{-1}, respectively. The last two values compare favorably with literature values of 1.1×10^{-3} M for the solubility of iodine in pure water[56] and 6.1×10^{-3} cm s^{-1} for the heterogeneous rate constant for dissolution of solid iodine in 10 mM KI solution.[11] The last parameter was necessary to modify the degree of inflection in the upper part of the voltammetric wave as shown in Figure 7. Excellent agreement is seen between theory and experiment in terms of current magnitude, wave position, and inflection, giving good evidence for the proposed reaction mechanism and values of the kinetic parameters k_f and k_{het}.

Finally, as a further probe, we investigated the use of ultrasonically generated emulsions to remove iodine from the electrode surface. Cyclic voltammetry of 1 and 10 mM aqueous solutions of potassium iodide in 0.125 M H_2SO_4 was performed under 19 W cm^{-2} ultrasound at a horn-to-electrode distance of 12 mm. This is shown in Figure 13. At the higher concentration, the voltammetry deviates from the expected steady-state behavior and heavy electrode passivation due to insulating iodine buildup leads to current falloff. When 10% (25 mL) of the aqueous solution was replaced with dichloromethane and the mixture was emulsified, steady-state behavior was achieved and is seen in Figure 13c. This was confirmed spectroscopically to be due to the dissolution of iodine from the platinum electrode, illustrating that sonoemulsion techniques are an effective alternative way of maintaining an iodine-free electrode. It is evident that both laser activation with mass transport enhancement provided by gravity fed channel flow and the mass transport increase and emulsion induced by ultrasound provide useful and parallel tools for probing the mechanism of iodide oxidation at platinum electrodes, particularly in the high-concentration region.

Conclusions

The solid iodine formed at platinum electrodes by the electrochemical oxidation of aqueous potassium iodide has been examined by AFM and shown to be easily removed by both laser activation and sonoemulsion techniques. When a clean electrode is maintained at steady-state, an oxidation mechanism is established as follows:

$$2I^-(aq) - 2e^- \rightleftharpoons I_2(aq) \quad \text{(i)}$$

$$I_2(aq) + I^-(aq) \rightleftharpoons I_3^-(aq) \quad \text{(ii)}$$

$$I_2(aq) \rightleftharpoons I_2(s) \quad \text{(iii)}$$

$$I^-(aq) + I_2(s) \rightarrow I_3^-(aq) \quad \text{(iv)}$$

where the formal redox potential for reaction i is 0.358 V vs SCE in 0.1 M H_2SO_4 and the equilibrium constant for reaction ii is 580 M^{-1}. Optimization of other kinetic parameters was achieved by fitting the theory to steady-state laser-activated waves under flow where solid iodine buildup is controlled by laser illumination. Best-fit values of the k_f rate constant of 1×10^5 mol^{-1} cm^3 s^{-1}, the solubility of I_2 (reaction ii) of 1.85×10^{-3} M, and the heterogeneous rate constant for reaction iv, k_{het}, of 1.6×10^{-3} cm s^{-1} were obtained. The benefits of laser activation in studying electrode processes that produce surface-active intermediates or products can be clearly seen.

Acknowledgment. We are grateful to the EPSRC for a studentship for R.P.A. and for financial support (Grant No. GR/M12247) under the Analytical Sciences program. We also thank COLCIENCIAS for a studentship for M.F.S and Jon C. Ball for the operation of the "Mathematica" PC software.

Appendix 1

Channel Flow Theory for a Disk Electrode. The Levich equation for the limiting current (I_{Levich}/A) in a channel flow cell for a rectangular electrode is given by

$$I_{Levich} = 0.925nF[X]w(Dx_e)^{2/3}\left(\frac{\upsilon_f}{h^2 d}\right)^{1/3} \quad \text{(A1.1)}$$

where n is the number of electrons transferred, F (C mol^{-1}) is the Faraday constant, [X] (mol cm^{-3}) is the bulk concentration of species X with diffusion coefficient D (cm^2 s^{-1}), w (cm) is the width of the electrode of length x_e (cm) in the flow direction, υ_f (cm^3 s^{-1}) is the solution flow rate, $2h$ (cm) is the cell height, and d (cm) is the cell width. Next we consider a disk electrode of radius r and divide it up into incremental strips of width dz as illustrated in Figure 14. By Pythagoras' theorem, the length of these strips is given by

$$x_e = 2\sqrt{r^2 - z^2} \quad \text{(A1.2)}$$

So by substitution into eq 1, the corresponding limiting current of each strip (I_{strip}) is therefore given by

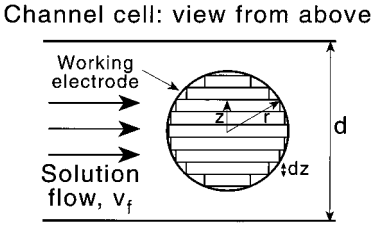

Figure 14. Schematic diagram for the consideration of a circular electrode as rectangular strips.

$$I_{\text{strip}} = 0.925nF[\text{X}]D^{2/3}\left(\frac{v_f}{h_2 d}\right)^{1/3}[2(r^2 - z^2)^{1/2}]^{2/3}\,\text{d}z \quad \text{(A1.3)}$$

The total current (I_{Tot}) is then defined as the sum of the currents from all the individual strips; that is,

$$I_{\text{Tot}} = \int_{-r}^{r} I_{\text{strip}} \quad \text{(A1.4)}$$

Since[58]

$$\int_{-r}^{r}(r^2 - z^2)^{1/3}\,\text{d}z = r^{5/3}\sqrt{\pi}[\Gamma(^4/_3)/\Gamma(^{11}/_{16})] \quad \text{(A1.5)}$$

$\Gamma(^4/_3) = 0.89338$, and $\Gamma(^{11}/_6) = 0.93969$,[59] then a new Levich equation for the current at a disk electrode (I_{disc}) of radius r in a flow cell can be established as

$$I_{\text{disc}} = 2.474nF[\text{X}]r^{5/3}D^{2/3}\left(\frac{v_f}{h^2 d}\right)^{1/3} \quad \text{(A1.6)}$$

Implicit in the above derivation is the neglect of diffusion in a direction orthogonal to x and y (see Figure 1, inset) so that the above derivation is limited to conditions of relatively fast electrolyte flow. By comparing the calculated current for a circular electrode with that for a square electrode with the same area using the above formulas in eqs A1.1 and A1.6, we see that the circular electrode has a ca. 2.3% larger current under channel flow.

References and Notes

(1) Lui, C.; Snyder, S. R.; Bard, A. J. *J. Phys. Chem. B* **1997**, *101*, 1180.
(2) Yaraliyev, Y. A. *Electrochim. Acta* **1984**, *29*, 1213.
(3) Thomas, A. E.; Wieckowski, A. *J. Electroanal. Chem.* **1995**, *399*, 207.
(4) Bittner, A. M.; Wintterlin, J.; Ertl, G. *J. Electroanal. Chem.* **1995**, *388*, 225.
(5) Lu, F.; Salaita, G. N.; Baltruschat, H.; Hubbard, A. T. *J. Electroanal. Chem.* **1987**, *222*, 305.
(6) Anson, F. C.; Lingane, J. J. *J. Am. Chem. Soc.* **1957**, *79*, 1015.
(7) Kolthoff, I. M.; Jordan, J. *J. Am. Chem. Soc.* **1953**, *75*, 1571.
(8) Lane, R. F.; Hubbard, A. T. *J. Phys. Chem.* **1975**, *79*, 808.
(9) Bejerano, T.; Gileadi, E. *J. Electrochem. Soc.* **1977**, *124*, 1720.
(10) Bejerano, T.; Gileadi, E. *J. Electroanal. Chem.* **1977**, *82*, 209.
(11) Desideri, P. G.; Lepri, L.; Heimler, D. *Encyclopaedia of the Electrochemistry of the Elements*; Bard, A. J., Ed.; Marcel Dekker: New York, 1976; Vol. 1, Chapter 3.
(12) Zakhodyakina, N. A.; Navitskii, M. A.; Sokolov, L. A.; Lukovtsev, P. D. *Elektrokhimiya* **1965**, *1*, 138, 251.
(13) Gokhshtein, A. Y. *Elektrokhimiya* **1965**, *1*, 285, 906.
(14) Tadayyoni, M. A.; Gao, P.; Weaver, M. J. *J. Electroanal. Chem.* **1986**, *198*, 125.
(15) Suárez, M. F.; Roberts, S. L.; Compton, R. G. Manuscript in preparation.
(16) Gao, X.; Weaver, M. J. *J. Am. Chem. Soc.* **1992**, *114*, 8544.
(17) Dané, L. M.; Janssen, L. J. J.; Hoogland, J. G. *Electrochim. Acta* **1968**, *13*, 507.
(18) Hinoue, T.; Watanabe, I.; Watarai, H. *Chem. Lett.* **1996**, *5*, 329.
(19) Chen, P. H.; McCreery, R. L. *Anal. Chem.* **1996**, *68*, 3958.
(20) Chen, P. H.; Frylung, M. A.; McCreery, R. L. *Anal. Chem.* **1995**, *67*, 3115.
(21) Jaworski, R. K.; McCreery, R. L. *J. Electrochem. Soc.* **1993**, *140*, 1360.
(22) McCreery, R. L.; Bowling, R.; Packard, R.; Poon, M. *Abstr. Pap.—Am. Chem. Soc.* **1988**, *196*, 185.
(23) Poon, M.; McCreery, R. L.; Engstrom, R. *Anal. Chem.* **1988**, *60*, 1725.
(24) Poon, M.; McCreery, R. L. *Anal. Chem.* **1987**, *59*, 1615.
(25) Poon, M.; McCreery, R. L. *Anal. Chem.* **1986**, *58*, 2256.
(26) Hershenhart, E.; McCreery, R. L.; Knight, R. D. *Anal. Chem.* **1984**, *56*, 2745.
(27) Oltra, R.; Indrianjafy, G. M.; Keddam, M.; Takenouti, H. *Corros. Sci.* **1993**, *35*, 827.
(28) Hinoue, T.; Harui, R.; Izumi, T.; Watanabe, I.; Watarai, H. *Anal. Sci.* **1995**, *11*, 1.
(29) Compton, R. G.; Dryfe, R. A. W. *Prog. React. Kinet.* **1995**, *20*, 245.
(30) Morrison, S. R. *Electrochemistry at Semiconductor and Oxidised Metal Electrodes*; Plenum: New York, 1980.
(31) Smalley, J. F.; Krishnan, C. V.; Goldman, M.; Feldberg, S. W.; Ruzic, I. *J. Electroanal. Chem.* **1988**, *248*, 255.
(32) Bechtel, J. H. *J. Appl. Phys.* **1975**, *46*, 1585.
(33) Aussel, J. D.; Le Brun, A.; Baboux, J. C. *Ultrasonics* **1988**, *26*, 245.
(34) Walton, D. J.; Phull, S. S. *Adv. Sonochem.* **1996**, *4*, 205.
(35) Compton, R. G.; Eklund, J. C.; Marken, F. *Electroanalysis* **1997**, *7*, 509.
(36) Marken, F.; Akkermans, R. P.; Compton, R. G. *J. Electroanal. Chem.* **1996**, *415*, 55.
(37) Klima, J.; Bernard, C.; Degrand, C. *J. Electroanal. Chem.* **1995**, *399*, 147.
(38) Compton, R. G.; Eklund, J. C.; Page, S. D.; Sanders, G. H. W.; Booth, J. *J. Phys. Chem.* **1994**, *98*, 12410.
(39) Marken, F.; Compton, R. G.; Bull, S. D.; Davies, S. G. *J. Chem. Soc., Chem. Commun.* **1997**, 995.
(40) Marken, F.; Compton, R. G. *Electrochim. Acta* **1998**, *43*, 2157.
(41) Compton, R. G.; Fisher, A. C.; Sanders, G. H. W. *Electroanalysis* **1993**, *5*, 615.
(42) Shuman, M. S. *Anal. Chem.* **1969**, *41*, 142.
(43) Jaworski, A.; Donten, M.; Stojek, Z.; Osteryoung, J. G. *Anal. Chem.* **1999**, *71*, 243.
(44) Beilby, A. I.; Crittenden, A. L. *J. Phys. Chem.* **1960**, *64*, 177.
(45) Compton, R. G.; Pilkington, M. B. G.; Stearn, G. M. *J. Chem. Soc., Faraday Trans.* **1988**, *84*, 2155.
(46) Bidwell, M. J.; Alden, J. A.; Compton, R. G. *J. Electroanal. Chem.* **1996**, *417*, 119.
(47) Rudolph, M. *J. Electroanal. Chem.* **1991**, *314*, 13.
(48) Rudolph, M. *J. Electroanal. Chem.* **1992**, *338*, 85.
(49) Cooper, J. A.; Compton, R. G. *Electroanalysis* **1998**, *10*, 141.
(50) Compton, R. G.; Eklund, J. C.; Page, S. D. *J. Phys. Chem.* **1995**, *99*, 4211.
(51) Mason, T. J.; Lorimer, J. P.; Bates, D. M. *Ultrasonics* **1992**, *30*, 140.
(52) Margulis, M. A.; Mal'tsev, A. N. *Russ. J. Phys. Chem.* **1969**, *43*, 592.
(53) Tang, H.; Kitani, A.; Shiotani, M. *J. Appl. Electrochem.* **1996**, *26*, 36.
(54) Chen, Y.; Zhang, H.; Wu, B. J. *Electroanal. Chem.* **1992**, *335*, 321.
(55) Beran, P.; Bruckenstein, S. *Anal. Chem.* **1968**, *40*, 1044.
(56) Swathirajan, S.; Bruckenstein, S. *J. Electroanal. Chem.* **1980**, *112*, 25.
(57) Akkermans, R. P.; Suárez, M. F.; Roberts, S. L.; Fulian, Q.; Compton, R. G. *Electroanalysis*, in press.
(58) Wolfram, S. *Mathematica, A System for Doing Mathematics by Computer*, 2nd ed.; Addison-Wesley: New York, 1991 (software package).
(59) Lide, D. R., Ed. *CRC Handbook of Chemistry and Physics*, 74th ed.; CRC Press: Boca Raton, FL, 1993.